

What's in Your Transit? Towards Reliably Getting 5 \times More Science from Exoplanet Transit Data

SAMSON J. MERCIER ,¹ JULIEN DE WIT ,¹ AND BENJAMIN V. RACKHAM ,^{1,2}

¹Department of Earth, Atmospheric and Planetary Sciences, Massachusetts Institute of Technology, 77 Massachusetts Avenue, Cambridge, MA 02139, USA

²Kavli Institute for Astrophysics and Space Research, Massachusetts Institute of Technology, Cambridge, MA 02139, USA

ABSTRACT

Exoplanetary science heavily relies on transit depth (D) measurements. Yet, as instrumental precision increases, the uncertainty on D appears to increasingly drift from expectations driven solely by photon-noise. Here we characterize this shortfall (the Transit-Depth Precision Problem, TDPP), by defining an amplification factor, A , quantifying the discrepancy between the measured transit-depth uncertainty and the measured baseline scatter on a same time bin size. While in theory A should be $\sim \sqrt{3}$, we find that it can reach values $\gtrsim 10$ notably due to correlations between D and the limb-darkening coefficients (LDCs). This means that (1) the performance of transit-based exoplanet studies (e.g., atmospheric studies) can be substantially improved with *reliable* priors on LDCs and (2) low-fidelity priors on the LDCs can yield substantial biases on D —potentially affecting atmospheric studies due to the wavelength-dependence of such biases. For the same reason, biases may emerge on stellar-density and planet-shape/limb-asymmetry measurements. With current photometric precisions, we recommend using a 3rd-order polynomial law *and* a 4th-order non-linear law, as they provide an optimal compromise between bias and A , while testing the fidelity for each parametrization. While their use combined with existing LDC priors (10–20% uncertainty) currently implies $A \sim 10$, we show that targeted improvements to limb-darkening models can bring A down to ~ 2 . Improving stellar models and transit-fitting practices is thus essential to fully exploit transit datasets, and reliably increasing their scientific yield by 5 \times , thereby enabling the same science with up to 25 \times fewer transits.

Keywords: Transmission spectroscopy (2133); Stellar atmospheres (1584); Planet hosting stars (1242); Exoplanet atmospheres (487); Fundamental parameters of stars (555)

1. INTRODUCTION

Since its launch, JWST has ushered in a new era of exoplanet science. Thanks to the unprecedented information content of its data, we can probe in finer detail the structure and composition of exoplanet atmospheres (e.g., [Xue et al. 2024](#); [Welbanks et al. 2024](#)) and investigate novel processes such as photochemistry (e.g., [Tsai et al. 2023](#); [Dyrek et al. 2024](#)), atmosphere–interior interactions (e.g., [Tsai et al. 2021](#); [Benneke et al. 2024](#)), and planetary oblateness (i.e., internal processes, e.g., [Berardo & de Wit 2022](#); [Liu et al. 2025](#)).

Although instrumentation has improved drastically over the last decades, the models and frameworks used to interpret data have lagged behind. One example is our incomplete understanding of stars: stellar magnetic active regions (spots and faculae) consistently contaminate photometric and spectroscopic observations (e.g., [Dumusque et al. 2011b,a](#); [Meunier et al. 2017](#); [Rackham et al. 2017, 2018, 2019, 2023](#); [Saba et al. 2025](#)).

Our inability to model or mitigate these effects leads to biased measurements of the radial velocity amplitude and transit depth from which the most basic exoplanet properties—mass and radius, respectively—are measured (e.g., [Rabus et al. 2009](#); [Carter et al. 2011](#); [Lovis et al. 2011](#)). Similar biases can arise from other model limitations, such as with line shape parameterizations in opacity models ([Niraula et al. 2022, 2023](#)). These model limitations propagate throughout our analyses and hamper our ability to draw meaningful conclusions on exoplanet characteristics.

In this context, here we examine the information content of exoplanet transit data with the goal of identifying what targeted improvements to methods and models can enhance the scientific return of these observations. In [Section 2](#), we present the root cause for our investigation, the “Transit-Depth Precision Problem” (TDPP). In [Section 3](#), we present the methodology developed to investigate its main origins and quantify their respec-

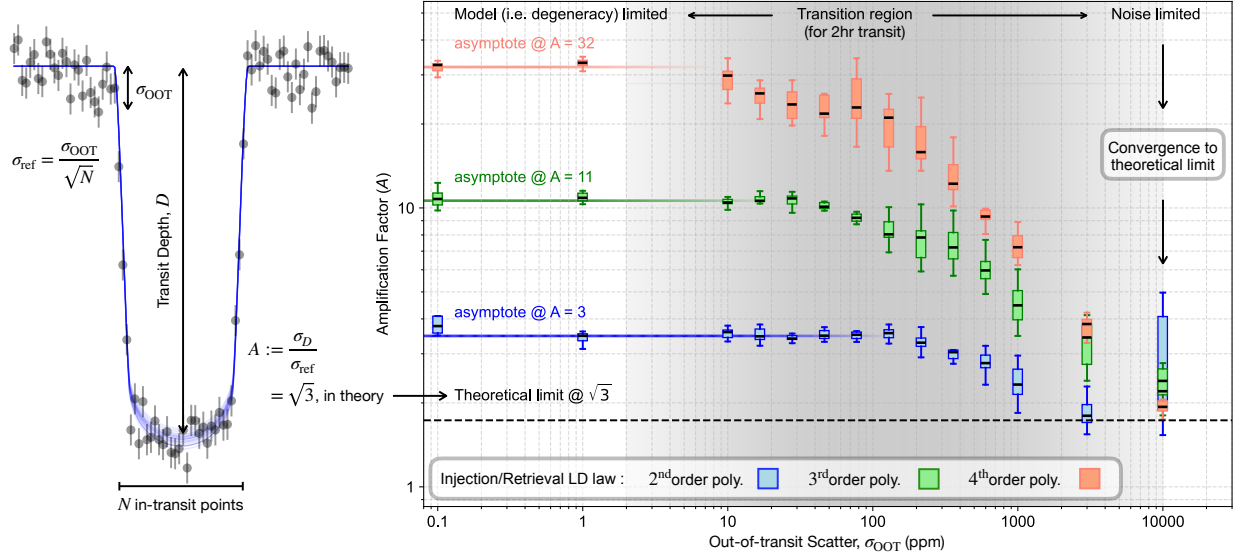


Figure 1. Expectations vs reality in constraining an exoplanet transit depth. *Top left:* Mock transit generated with the properties listed in Table 1. Black points show the light curve with 600 parts per million (ppm) of injected Gaussian white noise. Blue curves are model realizations drawn from the posterior distribution of D obtained by fitting this dataset. Annotated arrows indicate the quantities relevant to the TDPP. *Right:* Illustration of the TDPP. Each coloured box plot set corresponds to injection–retrieval tests done with a different limb-darkening prescription. For each set the injection and retrieval models have the same functional form. Box plots summarize 10 MCMC retrievals with identical scatter but different noise realizations. The shaded horizontal line within the boxes marks the distribution’s median, while the lower and upper box edges correspond to its first and third quartiles. Whiskers, denoting the minimum and maximum values, are calculated as $1.5 \times$ the first and third quartile. The regimes and asymptotic behaviours of these injection–retrieval families are discussed in Section 2. The injected out-of-transit scatter (σ_{OOT}) is measured in 120-min bins.

tive contributions. We discuss in Section 4 targeted strategies to mitigate their respective effects and present the substantial boost in scientific return the community could then expect. We conclude in Section 5.

2. THE TRANSIT-DEPTH PRECISION PROBLEM

Transit observations have played a central role in advancing exoplanet science. The most informative observable for atmospheric science across the board is the transit depth, $D = (R_p/R_*)^2$, in which R_p is the planetary radius and R_* is the stellar radius. Measuring D at different wavelengths reveals the planet’s apparent size as a function of wavelength, which can be translated into information on atmospheric opacity (e.g., Seager & Sasselov 2000; Benneke & Seager 2012; de Wit & Seager 2013). The precision with which D is measured directly sets the limit on the inferences that can be made about atmospheric characteristics (e.g., Deming et al. 2009; Greene et al. 2016). It is thus crucial that the uncertainty on the transit depth (σ_D) be minimized—as well as biases on it, naturally.

To first order, one could expect that σ_D relates to the scatter in the photometric time series (Figure 1, left panel), which includes both photon noise (roughly Gaussian at high count levels) and correlated noise (marginal to first order), measurable as the out-of-transit scatter

for a bin of duration similar to the transit duration ($\sigma_{\text{ref}} = \sigma_{\text{OOT}}/\sqrt{N}$ with N in-transit points). Specifically, one expects that $\sigma_D \simeq \sqrt{3} \sigma_{\text{ref}}$ as the typical out-of-transit baseline for transit observations is twice the duration of the transit event targeted. However, when comparing these two quantities in many existing datasets, a significant discrepancy between expectation and reality emerges (i.e., $\sigma_D/\sigma_{\text{ref}} \gg \sqrt{3}$). We define the amplification factor $A = \sigma_D/\sigma_{\text{ref}}$, which we use hereafter to investigate this discrepancy.

We illustrate this discrepancy through a set of injection–retrieval tests, whose results are shown in the right panel of Figure 1. For these tests, we simulated a single transit with the `squishyplanet` package (Cassese et al. 2024) using GJ 1214’s properties and varying levels of white noise, before fitting the mock data with the same package. The transit is constructed with equal pre-, post- and in-transit durations (as in Figure 1, left panel). To sample the posterior, we used the Affine Invariant Markov Chain Monte Carlo (MCMC) method implemented in the `emcee` package (Foreman-Mackey et al. 2013) with 50 walkers run for 100,000 steps, discarding the first 70,000 as burn-in. We applied uninformative uniform priors to all fitted parameters except the orbital period, on which we set a strong Gaussian prior, and the transit midpoint, which was

fixed. This setup reflects the fact that such analyses generally assume prior observations have tightly constrained transit timings. Walkers were initialized in a wide multi-dimensional Gaussian ball around truth. To exclude poorly converged chains, we performed both automated chain sigma clipping and manual walker rejection. From D 's posterior we measured σ_D , and with the injected white noise level we computed the corresponding A . Further details can be found in Table 1.

Each coloured box plot set in the right panel of Figure 1 highlights injection–retrieval tests done with a specific limb-darkening prescription. The behaviour of these sets falls into three regimes. At high scatter, the amplification factor approaches the theoretical limit of $\sqrt{3}$, indicating that the retrievals are noise-limited. At low scatter values, the amplification plateaus. This plateau is driven by degeneracies and correlations among our model's parameters. Indeed, when fitting transits, parameters describing the exoplanet's orbit and the stellar intensity profile must be inferred alongside the transit depth. Many of these parameters affect the transit shape in similar ways, producing compensatory effects where different parameter combinations yield similar light curves (see, e.g., Figure 2 and de Wit et al. 2012, Fig. 4). Such interdependence broadens the posterior distribution for D , increasing A . The magnitude of the model-driven change in A depends of the dimensionality of the retrieval. As more model parameters are included, for example when moving from a second- to a fourth-order polynomial limb-darkening law (LDL), the space of iso-probability solutions expands, thus broadening the posterior distributions. Finally, between these two regimes is a transition wherein retrievals shift from being noise- to model-limited.

3. CAUSE OF THE AMPLIFICATION FACTOR

As discussed in Section 2, when leaving the noise-limited regime ($\sigma_{\text{OOT}} \lesssim 3000$ ppm), degeneracies between model parameters drive A . In this section, we present an analysis of the origins of the TDPP.

3.1. Selecting an appropriate parameterization

All light curves generated for this section's analyses were produced using a fourth-order non-linear LDL. This prescription has been shown to provide the most accurate estimate of stellar intensity profiles and currently appears to be the most appropriate choice for precise transit observations (e.g., Espinoza & Jordán 2016, hereafter EJ16, Morello et al. 2017; Keers et al. 2024). We derived corresponding LDCs for GJ 1214 by combining its stellar properties with the ExoTic-LD package (Grant & Wakeford 2024) and MPS-ATLAS set1 grid

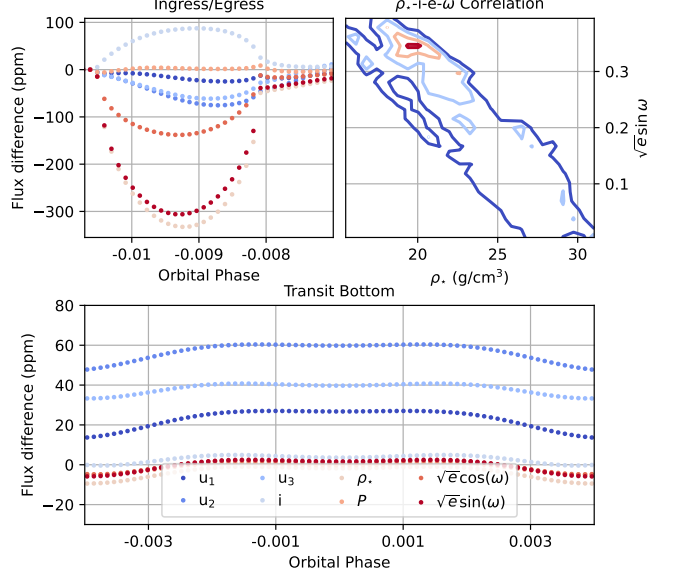


Figure 2. Parameter perturbations on transit shape. Separate panels highlight the transit ingress/egress, and bottom. Symmetric “bumps” can be clearly seen at ingress and egress, driven by the orbital parameters. In contrast, fluctuations in the bottom are dominated by the LDCs. Perturbations beyond the photometric precision (16 ppm here) are due to underlying correlation, e.g., between ρ_* vs $\sqrt{e} \sin \omega$ (top-right). In practice, these correlations link all orbital parameters. The coloured contours indicate the 10, 30, 60, and 90% equi-probability levels.

(Kostogryz et al. 2022). This grid provides up-to-date stellar models and yields coefficients consistent with its MPS-ATLAS set2 counterpart (Kostogryz et al. 2023).

While the generated data are designed to resemble observations, the chosen limb-darkening model must balance dimensionality with the potential bias introduced by over-simplifying the parameterization. In Section 4, we found that a third-order polynomial LDL offers the best compromise between bias and complexity.

3.2. Perturbation analysis

The model-driven increase in A results from correlations between transit model parameters. Different combinations can generate nearly identical light curves, making it difficult to disentangle each parameter's contribution and recover its true value. A simple way to illustrate this effect is to perturb each parameter by 1σ after fitting and examine how the light curve responds, an approach previously used by de Wit et al. (2012) to study secondary eclipses. We present the results of this perturbation analysis in Figure 2, specifically focusing on changes in the transit ingress/egress (top left panel), and bottom (bottom panel).

At ingress and egress, perturbations generate symmetric bumps, with orbital parameters producing the largest

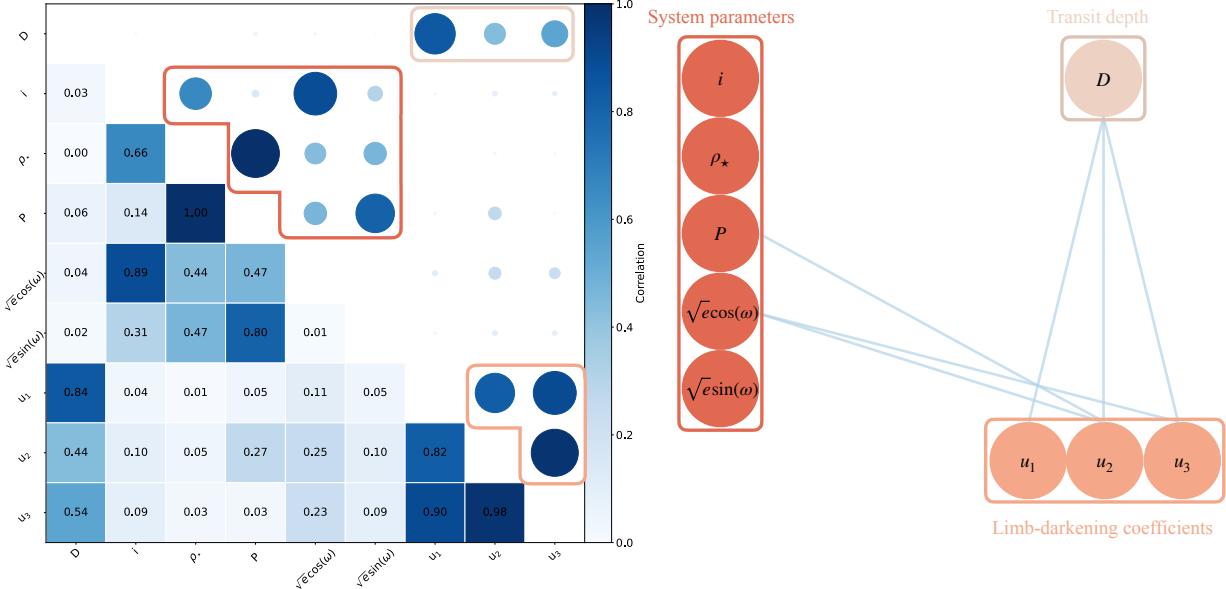


Figure 3. Revealing underlying network of correlations. Results of the sensitivity analysis. *Left:* Correlation matrix. The lower triangle reports correlation values derived from χ^2 maps, with shading scaled to the absolute values. The upper triangle provides a circular representation of the same matrix, where circle size and shading scale with correlation strength, making the families of correlated parameters easier to distinguish. The transit depth is by far most strongly correlated with u_1 , u_2 , and u_3 . *Right:* Network representation of the correlations. Parameters are grouped into families using the same colour scheme as in the matrix. Blue lines highlight the strongest links between parameters of different families.

changes. This is expected: fixing the transit midpoint and varying the orbital parameters is equivalent to altering the transit duration (Seager & Mallén-Ornelas 2003). Parameters that induce similar bumps (to first order), like the stellar density (ρ_*) and $\sqrt{e} \sin \omega$, are correlated (illustrated in Figure 2 top right panel). These relationships complicate posterior sampling, as algorithms like MCMC or nested sampling must navigate a landscape filled with local minima (or narrow “valleys”). In contrast, LDCs have a weak impact on the transit wings; variations in the LDCs impact the intensity profile but not the transit duration.

The picture is different in the transit bottom. Orbital parameters induce modest changes (~ 0 – 10 ppm), whereas perturbations to the LDCs shift the bottom by ~ 20 – 60 ppm. This reflects the role of limb-darkening in shaping the overall depth and curvature of the transit bottom. The three coefficients produce nearly identical patterns, differing only in amplitude. Since D is predominantly measured from the transit bottom, these results imply that LDCs are the main drivers of the TDPP.

3.3. Sensitivity analysis

To quantify parameter correlations and their impact on D , we carried out a targeted sensitivity analysis. The challenge here is to isolate correlations between pairs of parameters. This cannot be done via cuts in the full multi-dimensional posterior space sampled by

an MCMC, as it would introduce biases from other dimensions. Instead, we evaluate the local χ^2 (or log-likelihood) space in two chosen dimensions at a time.

For each pair, we generated a light curve, injected 16 ppm of white noise (model-limited regime), and computed the χ^2 across a grid values centered on truth. Because our injection–retrieval tests use different LDLs (see Section 3.1), we define “truth” for the LDCs as the best-fit values from fitting the injected non-linear LDL intensity profile with the 3rd-order polynomial LDL.

Elliptical equi- χ^2 contours were then overlaid to each map. The rotation angle θ of each ellipse encodes the space’s orientation, which we translated into a correlation metric $c = \sin(2\theta)$. c peaks for diagonal contours (i.e., strong correlation) and reaches a minimum for vertical or horizontal contours (i.e., no correlation).

The results are summarized in Figure 3, and the full set of χ^2 maps is provided in Figure 5. The left panel presents the correlation matrix, from which two conclusions can be drawn. First, transit depth is most strongly correlated with the LDCs, confirming that they dominate the amplification factor and the TDPP. Second, two families of correlations can be distinguished: one linking orbital parameters and another the LDCs. However, these two families are not entirely isolated: there are clear correlations between their members, such as between $\sqrt{e} \sin \omega$, i , ρ_* , u_2 , and u_3 —corresponding to the “e-b- ρ -BD” (for brightness distribution) correlation

introduced in [de Wit et al. \(2012\)](#). This mirrors what we observed in [Figure 2](#), where correlated parameters (either within each family or across them) produced similar perturbations in transit shape. The right panel re-frames these findings in a digestible network form.

Together the perturbation and sensitivity analyses paint a consistent picture: transit depth is most strongly coupled to the LDCs. This makes them the central bottleneck in improving transit depth precision measurements, and underscores the need for tighter external constraints through improved stellar models or spectroscopic characterization. Interestingly, this contrasts with the findings of [Morris et al. \(2020\)](#) who reported that the impact parameter had the strongest influence on the transit depth.

4. RELIABLY BOOSTING TRANSIT SCIENCE

LDCs are the leading drivers in the TDPP. In the following section we discuss mitigation strategies for constraining these coefficients and illustrate the improvements that such strategies could have on reducing A .

4.1. *Constraints from stellar models*

A common practice when fitting transits is to constrain LDCs using estimates derived from stellar models. Tools such as `ExoTiC-LD` or `ExoCTK` ([Bourque et al. 2021](#)) provide LDC estimates based on stellar parameters and a given stellar atmospheric model. While these estimates are convenient, it is important to remain cautious about biases introduced when relying on these model-derived LDCs in transit fits. Indeed, [Espinoza & Jordán \(2015\)](#) (hereafter [EJ15](#)) and [EJ16](#) have shown that LDCs vary significantly between stellar models. Additionally, [EJ15](#), [EJ16](#), and [Howarth \(2011\)](#) warn that model-derived LDCs differ from ones measured from photometric observations. Using model-derived LDCs without caution can therefore introduce systematic biases that depend on the stellar type and exoplanet orbital configuration.

[EJ15](#) and [EJ16](#) highlight two other critical points: LDCs should not be fixed to model values but allowed to float during fitting; and that some models, such as ATLAS9 ([Kurucz 1979](#)), better reproduce photometric LD than others, like PHOENIX ACES ([Husser et al. 2013](#)). While the studies caution against the blind use of model-derived LDCs, they also show that such outputs still provide good order-of-magnitude estimates of the values expect from photometry (Figs. 8 & 9 of [EJ15](#)).

Motivated by these insights, we perform a series of tests in which we fit simulated light curves while varying both the number of free LDCs and the priors imposed on them. Our goal is to illustrate the impact that vary-

ing limb-darkening parameterizations can have on reducing the amplification factor. We adopt the modern MPS-ATLAS set1 and set2 stellar models ([Kostogryz et al. 2022, 2023](#)) as our fiducial stellar models, since they outperform older grids. However, we note that a full sensitivity analysis comparing all available models to photometric measurements, similar to that in [EJ15](#), remains necessary to fully validate model-derived LDCs from the MPS-ATLAS sets.

To estimate the strength of priors that can reasonably placed on LDCs using the MPS-ATLAS models, we compared their outputs across the full parameter range (i.e., $T_{\text{eff}} \in [3500, 9000]$ K, $\log g \in [3.0, 5.0]$, and $[\text{M}/\text{H}] \in [-5.0, 1.5]$). We used `ExoTiC-LD`, which generates intensity profiles by combining stellar model intensities with an instrument throughput and integrating over a specified wavelength range. For convenience, we selected JWST’s NIRSpec PRISM. The resulting intensity profiles were then fit with a fourth-order non-linear LDL. We quantified the relative differences in the resulting LDCs by taking the median of their distributions (see [Figure 6](#)). From this analysis, we find that the relative differences between the two MPS-ATLAS grids are on the order of 10–20%. Consequently, the tightest priors that can currently be placed on LDCs from state-of-the-art stellar models are Gaussian priors with widths of $\sim 10\text{--}20\%$. By contrast, when comparing the MPS-ATLAS-derived LDCs to those produced by other stellar model grids—namely PHOENIX ([Husser et al. 2013](#)), Stagger ([Magic et al. 2013](#)), and Kurucz ([Kurucz 1979](#))—we find relative differences of 15–90%. This highlights not only the inconsistencies across available stellar models but also that the choice of model has a strong impact on the LDC constraints and the measured transit depth.

4.2. *Impact of priors and LDL choice*

[Figure 4](#) presents the results of our injection–retrieval tests. The mock light curves were generated with a fourth-order non-linear LDL (as discussed in [Section 3.1](#)) and injected with 16 ppm of Gaussian white noise. This noise level was chosen to ensure the retrievals operate in the model-limited regime (see [Figure 1](#)). Retrievals were performed using polynomial LDLs of order 2, 3, 4, 5, 6, and 9, as well as with a fourth-order non-linear LDL. Aside from the choice of LDC priors, the model setup, posterior sampling and post-processing procedures were identical to those used in the injection–retrieval tests of [Section 2](#).

We highlight four main conclusions from [Figure 4](#). First, the often-used second-order polynomial LDL is inadequate. While it achieves relatively low amplification

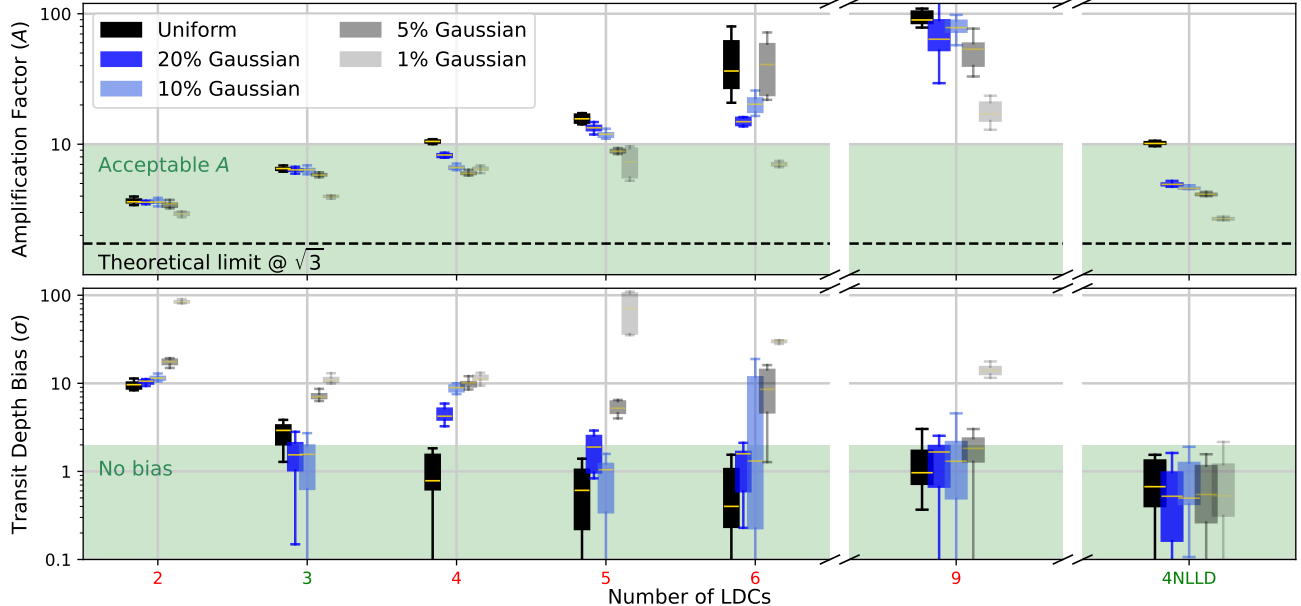


Figure 4. Towards optimal limb-darkening parametrization. Amplification factor (top) and transit depth bias (bottom) from our injection–retrieval tests. Results are shown as a function of the number of LDCs (x-axis) under different limb-darkening priors assumptions, ranging from uninformative uniform priors to Gaussian priors of varying widths. Polynomial LDLs are used for cases with 2–9 LDCs, while “4NLLD” refers to the fourth-order non-linear LDL. Since this is the law for injection, it yields the best performance. Priors informed by current stellar models are highlighted in blue (typical relative uncertainties between 10 and 20%). As in Figure 1, the black dashed horizontal line marks A ’s theoretical limit, and box plots summarize the results from 10 MCMC retrievals with different noise realizations. Green vertical bands indicate the regimes considered acceptable: for the bias, results within 2σ of truth and for the amplification factor, $A < 10$. As discussed in Section 4.2, given these acceptability criteria we highlight the optimal limb-darkening parameterizations with green x-axis labels, and the sub-optimal ones in red.

factor, it results in a strong bias on D ($\geq 10\sigma$). In other words, simply constraining the LDCs is not enough: if the chosen LDL’s fidelity level is insufficient, large biases are unavoidable.

Second, for polynomials of third-order and higher, retrievals become more reliable. They results in bias $\leq 2\sigma$ when paired with priors at the level current achievable from stellar models. The third-order polynomial LDL represents a practical “sweet spot”: it is flexible enough to capture the true intensity distribution without introducing excessive degeneracy, but not so high in dimensionality that the amplification factor becomes unmanageable. At still higher orders (fourth and greater), the added degrees of freedom inflate the amplification factor ($A > 10$) while providing no compensating gain in accuracy, making them suboptimal in practice.

Third, turning to the fourth-order non-linear LDL, the results are as expected. This law performs the best since it functionally matches the injection model (“perfect” model fidelity, meaning that no compensation is needed). It results in the lowest transit depth bias, with the median (yellow line in each box plot) consistently below 1σ , and strongest reduction in A across prior strengths. In particular, placing Gaussian priors of 10–20% widths reduces the amplification factor by a

factor of two, and pushing priors down to 1% widths—potentially achievable with future stellar models—yields a five-fold decrease. Such gains in transit depth precision translate to requiring 4–25× fewer transits to achieve the same level of scientific return (e.g., placing constraints on atmospheric properties from transmission spectra).

Finally, the trends observed when varying the prior strength are instructive. For A , tighter priors consistently reduce the amplification factor, as expected: narrower priors constrain both the LDCs and transit depth posterior distributions. In contrast, biases increase as priors tighten. This arises from the way prior means are defined. For polynomial LDL retrievals, priors are centered on the coefficients obtained when fitting the injected non-linear intensity profile with the polynomial law (as in Section 3.3). Because polynomial LDLs cannot perfectly reproduce the non-linear law—especially at low orders—the LDCs are intrinsically biased from “truth”. When priors are tightened around these erroneous estimates, the MCMC chains are confined to biased regions of parameter space. To compensate for this, other parameters such as the transit depth are adjusted, leading to larger biases in the retrieved properties.

Taken together, these results suggest that observers should fit modern light curves with both a third-order

polynomial and fourth-order non-linear LDL. Both prescriptions provide optimal compromise between A and bias, while also serving as useful cross-checks: their distinct functional forms make them sensitive to different aspects of the stellar intensity profile, enabling a more complete characterization of the underlying stellar properties. As a community, we should therefore encourage the use of multiple LDLs when fitting light curves and recommend reporting of results from each prescription to highlight whether transit depth measurements differ or remain consistent across models.

5. CONCLUSION

Here we have examined why the precision of exoplanet transit depth measurements often falls short of the theoretical expectations set by the quality of the data, a shortfall we define as the TDPP. Through injection-retrieval simulations, we show that the uncertainty on D is systematically amplified by a factor of $A \gg \sqrt{3}$ relative to σ_{ref} . In fact, given current precisions on light-curves and LDCs/LDLs, we find that $A \sim 10$ generally. We recommend reporting the derived A values in future studies as a sanity check: $A \gg 10$ would imply that tighter constraints are likely accessible, while $A \ll 10$ would imply that the constraints on D are artificially tight and associated inferences may be biased.

Our perturbation-sensitivity analyses reveal that $A \gg \sqrt{3}$ originates from the correlation between the D and other model parameters, notably the LDCs. These correlations broaden the posterior distribution for D by factors that depend on the chosen LDL, the number of LDCs allowed to vary, and the priors applied. We find that Gaussian priors on LDCs can substantially reduce the amplification factor. Though existing models can reliably yield 10–20% precision on LDCs, upgrades bringing these values down to $\sim 1\%$ could reduce A to ~ 2 . Improving stellar models and transit-fitting practices can thus reliably increase the scientific yield of transit datasets by 5×—accomplishing the same science with up to 25× fewer transits.

Among the LDLs tested, our results disfavour the quadratic law, which introduces large transit depth biases ($\geq 10\sigma$), instead favouring the third-order polynomial and fourth-order non-linear LDLs. Both provide the best compromise between A and bias induced on the transit depth. With model-informed LDC priors, they yield A of ~ 5 –7 while incurring negligible transit depth bias ($< 2\sigma$). This aligns with previous studies showing that more flexible laws outperform the quadratic law in reproducing stellar intensity profiles (e.g., EJ16, Morello et al. 2017, Keers et al. 2024).

We also show that additional non-transit observations, such as radial velocity monitoring, cannot meaningfully mitigate the TDPP because they do not constrain the stellar intensity profile that shapes the transit light curve. Instead, progress will come from improved stellar models and novel limb-darkening parameterizations that reduce intra-LDC correlations (e.g., selecting more orthogonal parameter bases). These developments will not only improve transit depth precision, but also enhance other inferences—such as ρ_* measurements—that inherit biases from LDC correlations.

Overall, our findings demonstrate that the limiting factor in transit depth precision is not instrumental but rather our ability to model the stellar photosphere accurately. Improving the fidelity of stellar atmosphere models, adopting best practices for choosing LDLs, and applying realistic, model-based priors on LDCs can significantly reduce the amplification factor. Such advances are necessary to bring transit depth uncertainties closer to the photon-noise floor and to fully exploit the information content of high-quality data from JWST and future observatories.

ACKNOWLEDGEMENTS

This material is based upon work supported by the European Research Council (ERC) Synergy Grant under the European Union’s Horizon 2020 research and innovation program (grant No. 101118581—project REVEAL). This material is based upon work supported by the National Aeronautics and Space Administration under Agreement No. 80NSSC21K0593 for the program “Alien Earths”. The results reported herein benefited from collaborations and/or information exchange within NASA’s Nexus for Exoplanet System Science (NExSS) research coordination network sponsored by NASA’s Science Mission Directorate. SJM acknowledges support from the Massachusetts Institute of Technology through the Praecis Presidential Fellowship and Desmond Fellowship.

Software: `astropy`¹(v6.1.6 Astropy Collaboration et al. 2013, 2018, 2022), `emcee`²(v3.1.6, Foreman-Mackey et al. 2013), `ExoTiC-LD`³(v3.2.0, Grant & Wakeford 2024), `Matplotlib`⁴(v3.10.0,

¹ <https://www.astropy.org>

² <https://emcee.readthedocs.io/en/stable/>

³ <https://exotic-lc.readthedocs.io/en/latest/>

⁴ <https://matplotlib.org>

Hunter 2007), `numpy`⁵(v1.26.4 Harris et al. 2020), `squishyplanet`⁶(v0.3.1, Cassese et al. 2024),

REFERENCES

Astropy Collaboration, Robitaille, T. P., Tollerud, E. J., et al. 2013, *A&A*, 558, A33, doi: [10.1051/0004-6361/201322068](https://doi.org/10.1051/0004-6361/201322068)

Astropy Collaboration, Price-Whelan, A. M., Sipócz, B. M., et al. 2018, *AJ*, 156, 123, doi: [10.3847/1538-3881/aabc4f](https://doi.org/10.3847/1538-3881/aabc4f)

Astropy Collaboration, Price-Whelan, A. M., Lim, P. L., et al. 2022, *apj*, 935, 167, doi: [10.3847/1538-4357/ac7c74](https://doi.org/10.3847/1538-4357/ac7c74)

Benneke, B., & Seager, S. 2012, *ApJ*, 753, 100, doi: [10.1088/0004-637X/753/2/100](https://doi.org/10.1088/0004-637X/753/2/100)

Benneke, B., Roy, P.-A., Coulombe, L.-P., et al. 2024, arXiv e-prints, arXiv:2403.03325, doi: [10.48550/arXiv.2403.03325](https://doi.org/10.48550/arXiv.2403.03325)

Berardo, D., & de Wit, J. 2022, *ApJ*, 935, 178, doi: [10.3847/1538-4357/ac82b2](https://doi.org/10.3847/1538-4357/ac82b2)

Bourque, M., Espinoza, N., Filippazzo, J., et al. 2021, The Exoplanet Characterization Toolkit (ExoCTK), 1.0.0, Zenodo, doi: [10.5281/zenodo.4556063](https://doi.org/10.5281/zenodo.4556063)

Carter, J. A., Winn, J. N., Holman, M. J., et al. 2011, *ApJ*, 730, 82, doi: [10.1088/0004-637X/730/2/82](https://doi.org/10.1088/0004-637X/730/2/82)

Cassese, B., Vega, J., Lu, T., et al. 2024, The Journal of Open Source Software, 9, 6972, doi: [10.21105/joss.06972](https://doi.org/10.21105/joss.06972)

Cloutier, R., Charbonneau, D., Deming, D., Bonfils, X., & Astudillo-Defru, N. 2021, *AJ*, 162, 174, doi: [10.3847/1538-3881/ac1584](https://doi.org/10.3847/1538-3881/ac1584)

de Wit, J., Gillon, M., Demory, B. O., & Seager, S. 2012, *A&A*, 548, A128, doi: [10.1051/0004-6361/201219060](https://doi.org/10.1051/0004-6361/201219060)

de Wit, J., & Seager, S. 2013, *Science*, 342, 1473, doi: [10.1126/science.1245450](https://doi.org/10.1126/science.1245450)

Deming, D., Seager, S., Winn, J., et al. 2009, *PASP*, 121, 952, doi: [10.1086/605913](https://doi.org/10.1086/605913)

Dumusque, X., Santos, N. C., Udry, S., Lovis, C., & Bonfils, X. 2011a, *A&A*, 527, A82, doi: [10.1051/0004-6361/201015877](https://doi.org/10.1051/0004-6361/201015877)

Dumusque, X., Udry, S., Lovis, C., Santos, N. C., & Monteiro, M. J. P. F. G. 2011b, *A&A*, 525, A140, doi: [10.1051/0004-6361/201014097](https://doi.org/10.1051/0004-6361/201014097)

Dyreka, A., Min, M., Decin, L., et al. 2024, *Nature*, 625, 51, doi: [10.1038/s41586-023-06849-0](https://doi.org/10.1038/s41586-023-06849-0)

Espinoza, N., & Jordán, A. 2015, *MNRAS*, 450, 1879, doi: [10.1093/mnras/stv744](https://doi.org/10.1093/mnras/stv744)

—. 2016, *MNRAS*, 457, 3573, doi: [10.1093/mnras/stw224](https://doi.org/10.1093/mnras/stw224)

Foreman-Mackey, D., Hogg, D. W., Lang, D., & Goodman, J. 2013, *PASP*, 125, 306, doi: [10.1086/670067](https://doi.org/10.1086/670067)

Grant, D., & Wakeford, H. R. 2024, *Journal of Open Source Software*, 9, 6816, doi: [10.21105/joss.06816](https://doi.org/10.21105/joss.06816)

Greene, T. P., Line, M. R., Montero, C., et al. 2016, *ApJ*, 817, 17, doi: [10.3847/0004-637X/817/1/17](https://doi.org/10.3847/0004-637X/817/1/17)

Harris, C. R., Millman, K. J., van der Walt, S. J., et al. 2020, *Nature*, 585, 357, doi: [10.1038/s41586-020-2649-2](https://doi.org/10.1038/s41586-020-2649-2)

Howarth, I. D. 2011, *MNRAS*, 418, 1165, doi: [10.1111/j.1365-2966.2011.19568.x](https://doi.org/10.1111/j.1365-2966.2011.19568.x)

Hunter, J. D. 2007, *Computing in Science & Engineering*, 9, 90, doi: [10.1109/MCSE.2007.55](https://doi.org/10.1109/MCSE.2007.55)

Husser, T. O., Wende-von Berg, S., Dreizler, S., et al. 2013, *A&A*, 553, A6, doi: [10.1051/0004-6361/201219058](https://doi.org/10.1051/0004-6361/201219058)

Keers, R. E., Shapiro, A. I., Kostogryz, N. M., et al. 2024, *ApJL*, 977, L7, doi: [10.3847/2041-8213/ad8b51](https://doi.org/10.3847/2041-8213/ad8b51)

Kostogryz, N., Shapiro, A., Witzke, V., et al. 2023, *Research Notes of the AAS*, 7, 39

Kostogryz, N., Witzke, V., Shapiro, A., et al. 2022, *Astronomy & Astrophysics*, 666, A60

Kurucz, R. L. 1979, *ApJS*, 40, 1, doi: [10.1086/190589](https://doi.org/10.1086/190589)

Liu, Q., Zhu, W., Zhou, Y., et al. 2025, *AJ*, 169, 79, doi: [10.3847/1538-3881/ad9b8c](https://doi.org/10.3847/1538-3881/ad9b8c)

Lovis, C., Dumusque, X., Santos, N. C., et al. 2011, arXiv e-prints, arXiv:1107.5325, doi: [10.48550/arXiv.1107.5325](https://doi.org/10.48550/arXiv.1107.5325)

Magic, Z., Collet, R., Asplund, M., et al. 2013, *A&A*, 557, A26, doi: [10.1051/0004-6361/201321274](https://doi.org/10.1051/0004-6361/201321274)

Mahajan, A. S., Eastman, J. D., & Kirk, J. 2024, *ApJL*, 963, L37, doi: [10.3847/2041-8213/ad29f3](https://doi.org/10.3847/2041-8213/ad29f3)

Meunier, N., Mignon, L., & Lagrange, A. M. 2017, *A&A*, 607, A124, doi: [10.1051/0004-6361/201731017](https://doi.org/10.1051/0004-6361/201731017)

Morello, G., Tsiaras, A., Howarth, I. D., & Homeier, D. 2017, *AJ*, 154, 111, doi: [10.3847/1538-3881/aa8405](https://doi.org/10.3847/1538-3881/aa8405)

Morris, B. M., Bobra, M. G., Agol, E., Lee, Y. J., & Hawley, S. L. 2020, *MNRAS*, 493, 5489, doi: [10.1093/mnras/staa618](https://doi.org/10.1093/mnras/staa618)

Niraula, P., de Wit, J., Gordon, I. E., Hargreaves, R. J., & Sousa-Silva, C. 2023, *ApJL*, 950, L17, doi: [10.3847/2041-8213/acd6f8](https://doi.org/10.3847/2041-8213/acd6f8)

Niraula, P., de Wit, J., Gordon, I. E., et al. 2022, *Nature Astronomy*, 6, 1287, doi: [10.1038/s41550-022-01773-1](https://doi.org/10.1038/s41550-022-01773-1)

Rabus, M., Alonso, R., Belmonte, J. A., et al. 2009, *A&A*, 494, 391, doi: [10.1051/0004-6361:200811110](https://doi.org/10.1051/0004-6361:200811110)

Rackham, B., Espinoza, N., Apai, D., et al. 2017, *ApJ*, 834, 151, doi: [10.3847/1538-4357/aa4f6c](https://doi.org/10.3847/1538-4357/aa4f6c)

⁵ <https://numpy.org>

⁶ <https://squishyplanet.readthedocs.io/en/latest/>

Rackham, B. V., Apai, D., & Giampapa, M. S. 2018, *ApJ*, 853, 122, doi: [10.3847/1538-4357/aaa08c](https://doi.org/10.3847/1538-4357/aaa08c)

—. 2019, *AJ*, 157, 96, doi: [10.3847/1538-3881/aaf892](https://doi.org/10.3847/1538-3881/aaf892)

Rackham, B. V., Espinoza, N., Berdyugina, S. V., et al. 2023, *RAS Techniques and Instruments*, 2, 148, doi: [10.1093/rasti/rzad009](https://doi.org/10.1093/rasti/rzad009)

Saba, A., Thompson, A., Yip, K. H., et al. 2025, *ApJS*, 276, 70, doi: [10.3847/1538-4365/ad8c3c](https://doi.org/10.3847/1538-4365/ad8c3c)

Seager, S., & Mallén-Ornelas, G. 2003, *ApJ*, 585, 1038, doi: [10.1086/346105](https://doi.org/10.1086/346105)

Seager, S., & Sasselov, D. D. 2000, *ApJ*, 537, 916, doi: [10.1086/309088](https://doi.org/10.1086/309088)

Tsai, S.-M., Innes, H., Lichtenberg, T., et al. 2021, *ApJL*, 922, L27, doi: [10.3847/2041-8213/ac399a](https://doi.org/10.3847/2041-8213/ac399a)

Tsai, S.-M., Lee, E. K. H., Powell, D., et al. 2023, *Nature*, 617, 483, doi: [10.1038/s41586-023-05902-2](https://doi.org/10.1038/s41586-023-05902-2)

Welbanks, L., Bell, T. J., Beatty, T. G., et al. 2024, *Nature*, 630, 836, doi: [10.1038/s41586-024-07514-w](https://doi.org/10.1038/s41586-024-07514-w)

Xue, Q., Bean, J. L., Zhang, M., et al. 2024, *ApJL*, 963, L5, doi: [10.3847/2041-8213/ad2682](https://doi.org/10.3847/2041-8213/ad2682)

APPENDIX

A. SYSTEM AND INJECTION-RETRIEVAL PARAMETERS

Table 1 provides the parameters of the injection-retrieval exercise discussed in Section 2.

Table 1. Injection-retrieval parameters

Parameters	Values	Reference
Injection		
R_P/R_*	0.11589 ± 0.00016	Mahajan et al. (2024)
i (degrees)	88.7 ± 0.1	Cloutier et al. (2021)
P (days)	$1.580404531^{+0.000000018}_{-0.000000017}$	Mahajan et al. (2024)
a/R_*	$14.97^{+0.12}_{-0.14}$	Mahajan et al. (2024)
e	0.1	This study
ω (degrees)	50	This study
u_1 (poly./non-linear)	0.1/0.83	This study
u_2 (poly./non-linear)	0.2/−0.4	This study
u_3 (poly./non-linear)	0.4/0.15	This study
u_4 (poly./non-linear)	0.3/−0.025	This study
T_0 (days)	0	This study
Parameters	Priors	Walkers
Retrieval		
R_P/R_*	$\mathcal{U}(0, 1)$	$\mathcal{U}(0.1, 0.15)$
i (degrees)	$\mathcal{U}(60, 90)$	$\mathcal{U}(88, 90)$
P (days)	$\mathcal{N}(1.580405, 0.000063)$	$\mathcal{U}(1.58035, 1.58035)$
a/R_*	$\mathcal{U}(0, 30)$	$\mathcal{U}(14, 16)$
$\sqrt{e} \cos(\omega)$	$\mathcal{U}(-1, 1)$	$\mathcal{U}(0, 0.3)$
$\sqrt{e} \sin(\omega)$	$\mathcal{U}(-1, 1)$	$\mathcal{U}(0, 0.3)$
u_1	$\mathcal{U}(-100, 100)$	$\mathcal{U}(0, 0.3)$
u_2	$\mathcal{U}(-100, 100)$	$\mathcal{U}(0.1, 0.3)$
u_3	$\mathcal{U}(-100, 100)$	$\mathcal{U}(0.2, 0.6)$
u_4	$\mathcal{U}(-100, 100)$	$\mathcal{U}(0.2, 0.4)$
T_0 (days)	N/A	Fixed

NOTE—Rather than adopting literature values, we set the eccentricity and argument of periastron to arbitrary values to explicitly visualize the effect of non-circular orbits on the amplification factor. Similarly, the LDCs were manually selected to systematically vary the order of injected LDL. Relying on literature values would have constrained us to on quadratic limb-darkening alone, preventing exploration of higher-order laws. The reported injection LDCs fall into two categories. The first corresponds to the coefficients used in Section 2’s injection-retrieval tests. In this case, the coefficients were consistent across all three tested laws (e.g., the 2nd-order polynomial LDL used [0.1, 0.2] while the third-order polynomial LDL used [0.1, 0.2, 0.4]). The second category corresponds to the the LDCs used for the fourth-order non-linear LDL, which was used as injection in Section 3 and Section 4’s analyses. Priors and walker starting positions for these tests are not reported as they depend on the case considered. The methodology used to selected the priors and walkers starter positions for a given choice of injection and retrieval LDL is detailed in the main text (e.g. Section 3.3 and Section 4.2).

B. SENSITIVITY χ^2 MAPS

Figure 5 presents the results of our sensitivity test.

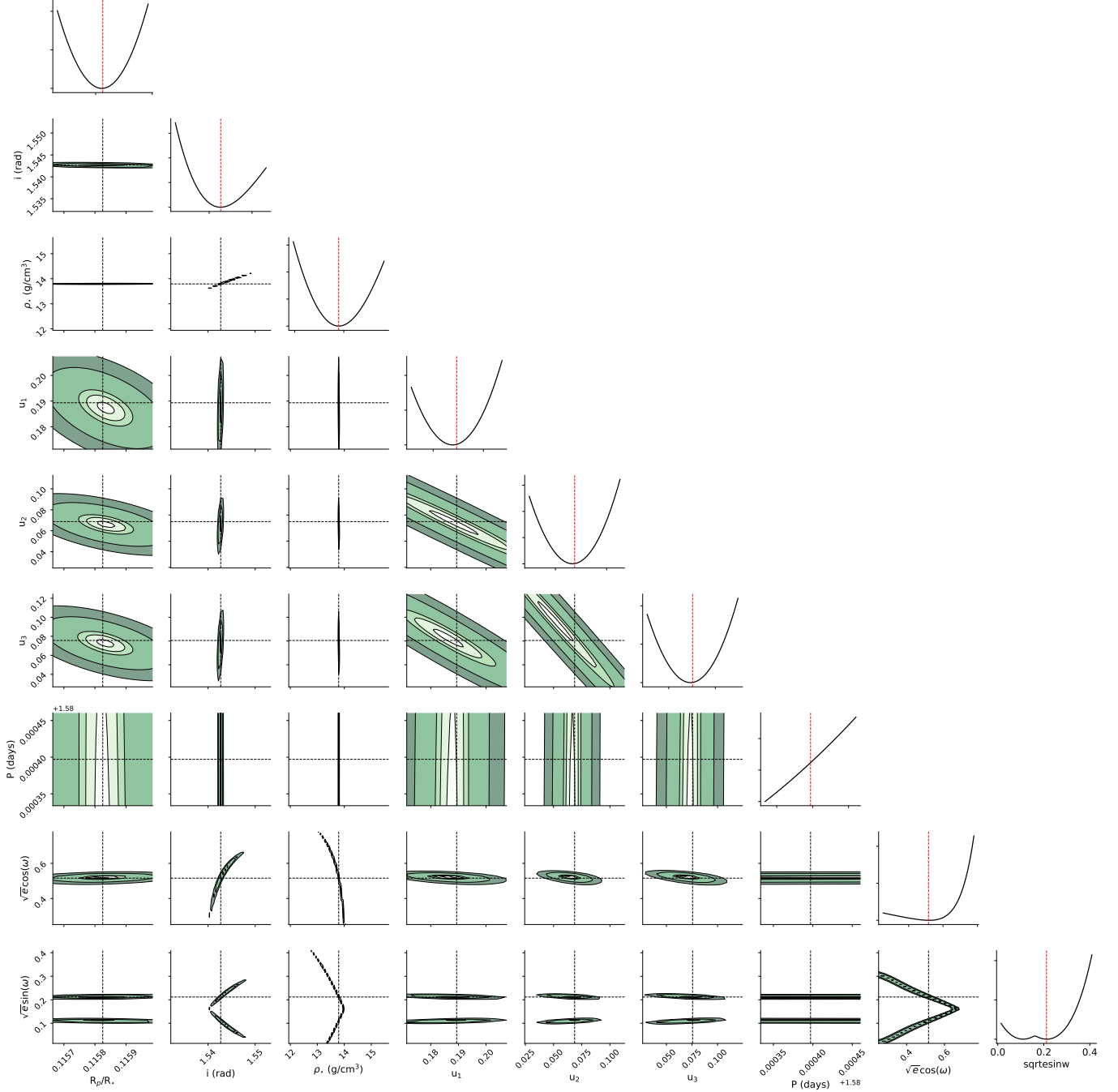


Figure 5. χ^2 maps across parameter pairs. Corner plot of the χ^2 maps used in our sensitivity test. Each diagonal subplot shows a 1-dimensional evaluation of the chi-squared space for the parameter corresponding to that column. Off-diagonal subplots display two-dimensional equi- χ^2 contours derived from the χ^2 maps, where each map was obtained by varying the parameters indicated on the x and y axes. Finally, for certain contours that are not elliptical (e.g., ρ_* versus P) we approximate them as first-order polynomials and compute the rotation angle using $\theta = \arctan(m)$, where m is the slope.

C. MODEL-DERIVED LDCS

Figure 6 presents the relative differences between fourth-order non-linear LDL coefficients as derived by the five stellar model grids available in ExoTiC-LD.

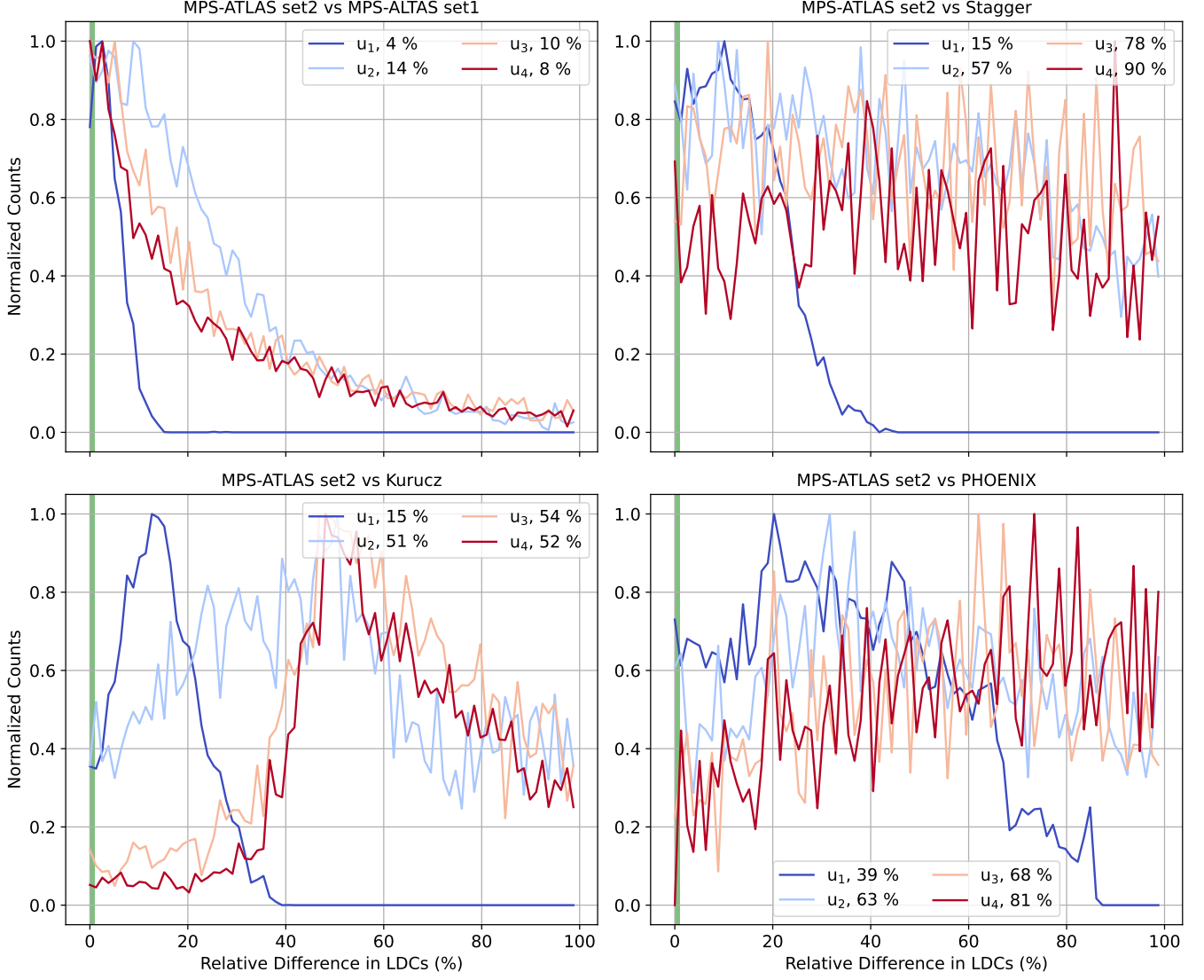


Figure 6. LDC differences across model grids. Each panel shows a normalized histogram of relative differences in the fourth-order non-linear LDL coefficients derived from the MPS-ATLAS set1 (Kostogryz et al. 2022), Stagger (Magic et al. 2013), Kurucz (Kurucz 1979), and PHOENIX (Husser et al. 2013) models against the MPS-ATLAS set2 (Kostogryz et al. 2023). Each coloured curve corresponds to a LDC, with the median value reported in the legend. The green vertical band marks the 1% level, indicating the threshold required to achieve a five-fold reduction in the amplification factor (see Figure 4 for details). While the MPS-ATLAS set1 and set2 models agree most closely, this reflects their internal precision rather than their accuracy. Indeed, they are consistent with one another but may still diverge from truth.